Journal of Materials Chemistry A



PAPER

View Article Online
View Journal



Cite this: DOI: 10.1039/d1ta05858d

a case study on thermoelectric V-VI nanoplates†

Scalable nanomanufacturing of chalcogenide inks:

Solution-processed semiconducting main-group chalcogenides (MMCs) have attracted increasing research interest for next-generation device technologies owing to their unique nanostructures and superior properties. To achieve the full potential of MMCs, the development of highly universal, scalable, and sustainable synthesis and processing methods of chalcogenide particles is thus becoming progressively more important. Here we studied scalable factors for the synthesis of two-dimensional (2D) V–VI chalcogenide nanoplates (M_2Q_3 : M = Sb, Bi; Q = Se, Te) and systematically investigated their colloidal behaviour and chemical stability. Based on a solvent engineering technique, we demonstrated scale-up syntheses of MMCs up to a 900% increase of batch size compared with conventional hydrazine-based gram-level syntheses, and such a scalable approach is highly applicable to various binary and ternary MMCs. Furthermore, we studied the stability of printable chalcogenide nanoparticle inks with several formulation factors including solvents, additives, and pH values, resulting in inks with high chemical stability (>4 months). As a proof of concept, we applied our solution-processed chalcogenide particles to multiple additive manufacturing methods, confirming the high printability and processability of MMC inks. The ability to combine the top-down designing freedom of additive manufacturing with bottom-up scalable synthesis of chalcogenide particles promises great opportunities for large-scale design and manufacturing of chalcogenide-based functional devices for broad application.

Received 11th July 2021 Accepted 3rd September 2021

DOI: 10.1039/d1ta05858d

rsc.li/materials-a

Introduction

Main-group chalcogens and metal chalcogenides containing sulfur (S), selenium (Se), or tellurium (Te) are versatile material platforms for energy conversion, 1-3 sensing, 4 and high-speed computing devices.^{5,6} For example, main-group chalcogenides (MMCs) have shown great promise in thermoelectric energy conversion including Bi₂Te₃, Sb₂Te₃, SnSe, and PbTe.⁷⁻⁹ Some prominent examples of thermoelectric MMCs not only demonstrate an excellent figure of merit (ZT) by themselves, 10 but also enable promising thermoelectric composites with other additive materials, such as carbon nanotubes. 11,12 A few MMCs also show intriguing phase-change properties and have been used in phase-change memory (PCM), leading to the development of solid-state drive and in-memory computing devices with sub-nanosecond writing (e.g., Sc_{0.2}Sb₂Te₃).¹³⁻¹⁵ The soft lattices of chalcogenides are both a blessing and curse: on the one hand, this leads to rich phase-transformation behaviors and associated property changes (e.g. electrical resistivity and

optical reflectivity) that can be exploited;^{16,17} on the other hand, such changes lead to complexities and uncertainties in their synthesis, in which impurity and undesired phases can occur in large-batch syntheses. Unlike metal oxides that can often be produced *via* scalable hydrolysis, the synthesis of MMCs often involves toxic ligands or reducing agents (*e.g.*, hydrazine and trioctylphosphine) to convert precursors into chalcogenides and maintain crystallinity with the necessity of inert atmospheres, limiting the potential for large-scale application in an industrial environment.

From an industrial nanomanufacturing perspective, an ideal synthesis process should include low cost precursors (stable and commercially available sources), benign starting materials (reagents with medium to low toxicity), and a high production yield (minimal impurity to avoid costly separation/purification processes). On an industrial scale, the energy input should also be carefully considered: highly scalable and controllable energy input (such as heat) should be prioritized, while expensive and small-scale energy sources (such as sonication energy) should be avoided. Last but not least, MMCs should be compatible with scalable device manufacturing techniques (such as additive manufacturing), which facilitates device fabrication from nanoscale building blocks to final products. Despite past efforts focusing on the MMC nanoparticle performance (e.g., electrical conductivity, band gap, etc.), to the

^eDepartment of Aerospace and Mechanical Engineering, University of Notre Dame, Notre Dame, IN 46556, USA. E-mail: yzhang45@nd.edu

^bDepartment of Chemistry, Northwestern University, Evanston, Illinois 60208, USA † Electronic supplementary information (ESI) available. See DO: 10.1039/d1ta05858d

synthesis scalability has rarely been systematically quantified, and more importantly the behavior of chalcogenide dispersion in practical application environments, such as in air and ink phases, is not well understood.

Here, we proposed a bottom-up approach to understand and address the research gap of converting nanoscale MMCs into macroscale devices in the context of scalable manufacturing and solution-based ink processing (Fig. 1a). We begin with the scalability analysis of different synthesis methods and propose a solvent engineering strategy to minimize the phase impurity during scale-up syntheses. Such a scalable manufacturing approach can be generalized for various one-dimensional and two-dimensional chalcogenide-based systems, including Te nanorods (1.40 \pm 0.42 μm in length), Bi₂Te₃ (0.96 \pm 0.11 μm), $Bi_2Te_{2.7}Se_{0.3}$ (0.87 \pm 0.27 μm), and Bi_2Se_3 (1.14 \pm 0.25 μm), as shown in Fig. 1b. To achieve high ink quality and stability, we investigated the effect of different ink formulations including solvents, pH values, and additives on the electrical conductivity of chalcogenide nanoparticles. By optimizing the ink formulation of MMCs, we are able to achieve MMC nanoplates with long-term chemical stability (>4 months). As a proof of concept, we applied our solution-processed chalcogenide particles to multiple additive manufacturing methods, demonstrating the high printability and processability of MMC-based inks.

We first systematically compared hydrazine-assisted colloidal synthesis (HCS), and solvent-engineered colloidal synthesis (ECS), and solvent-engineered colloidal synthesis (SCS) with regard to their scalability (a detailed comparison of these methods can be found in Table S1†). As a reducing agent, hydrazine has historically been used to synthesize metal chalcogenide nanoparticles from precursors due to its strong reductive capability and ease of separation (oxidation product of hydrazine is nitrogen gas). Despite previous successes in small-batch Sb_2Te_3 synthesis using toxic hydrazine, we found it quite challenging to scale up hydrazine-assisted colloidal synthesis as we observed the existence of impurities in final

products. As shown in Fig. 2a, the SEM image of moderate scaleup of HCS leads to a significant amount of tellurium nanowires as undesired byproducts. Past studies have suggested that Te is an intermediate product during Sb₂Te₃ synthesis, where Te can undergo disproportion in alkali medium to form Te²⁻ which then transforms into Sb₂Te₃ nanoplates.^{23,24} To allow the disproportion reaction proceed to completion, the choice of reaction conditions is important.25 We tested the reaction procedure with the same starting materials in EG without hydrazine (i.e., ECS method) and surprisingly observed a lower amount of Te nanowires formed during synthesis (Fig. 2b). It is worth mentioning that the solvent EG can behave as a reducing agent at elevated temperature. Some studies have suggested that ethylene glycol can be oxidized to glycolaldehyde and glycolate.26,27 As glycolaldehyde has a lower boiling point of 131.3 °C, an elevated temperature may help the removal of the oxidation product glycolaldehyde from the system. According to Le Chatelier's principle, any change in the status quo prompts an opposing reaction in the responding system. To further facilitate the reaction, the reaction temperature is elevated by solvent composition engineering through applying mixed solvents of EG and diethylene glycol (DEG). As shown in the SEM image (Fig. 2c), pure-phase Sb₂Te₃ nanoplates were obtained without observable Te nanowires. Furthermore, X-ray diffraction (XRD) analyses were performed to evaluate the phase purity of Sb₂Te₃ nanoplates by HCS, ECS, and SCS methods. As shown in Fig. 2d, SCS-synthesized Sb₂Te₃ nanoplates show an almost identical XRD peak pattern to reference XRD from the Inorganic Crystal Structure Database (ICSD), whereas there is a noticeable Te peak for HCS and ECS methods. In particular, HCS showed high Te signals with I_{Te} - $:I_{\mathrm{Sb2Te3}}$ reaching above 1.6 (Fig. 2e). Although anhydrous EG has a relatively high boiling point of 197 °C, the EG-based reaction mixture in a scale-up batch shows a lower reflux temperature (under 1 atm) due to the existence of volatile compounds (e.g., water produced from the reaction). The

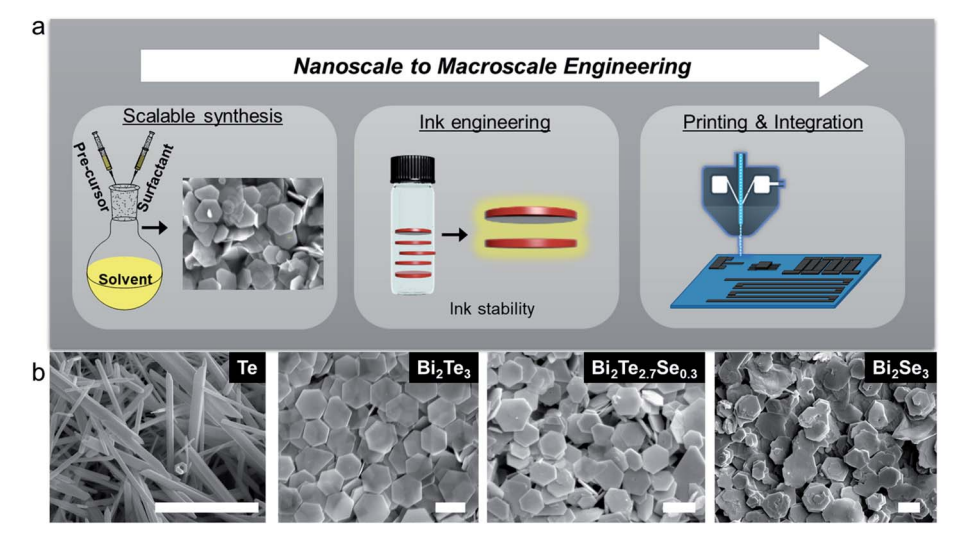


Fig. 1 The bottom-up strategy of scalable chalcogenide synthesis for printable inks. (a) Schematic illustration of scalable nanoparticle synthesis, ink engineering, and additive manufacturing. (b) Examples of chalcogen and chalcogenide systems from colloidal synthesis. Scale bars are 1 µm.

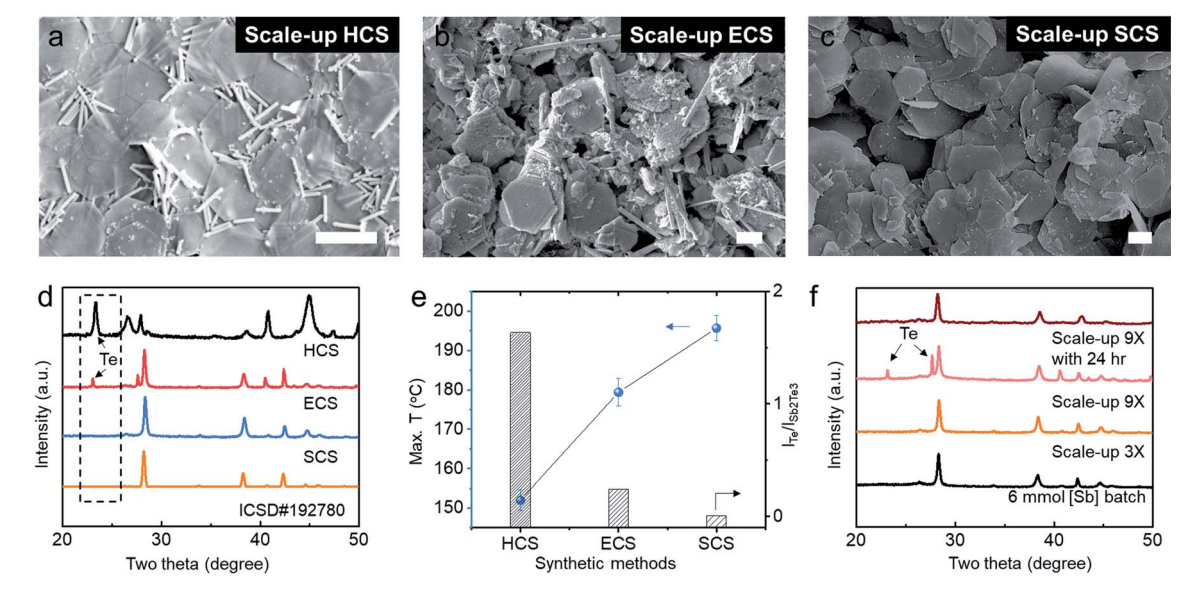


Fig. 2 Scalability analyses of different colloidal synthesis approaches. (a-c) SEM images of HCS (a), ECS (b), and SCS (c) in a scale-up batch. (d) XRD of Sb_2Te_3 nanoplates synthesized by HCS, ECS, and SCS approaches. (e) The relationship between the maximum reaction temperature and the amount of excess Te (characterized by the ratio of I_{Te} : I_{Sb,Te_3}). (f) XRD of Sb_2Te_3 nanoplates on different scales. Scale bars are 1 μ m.

maximum reaction temperatures of these three methods are recorded, as shown in Fig. 2e, revealing an opposite trend of increasing reaction temperature vs. impurity amount (Te). This is consistent with Le Chatelier's principle, which indicates that a higher reaction temperature facilitates overall chalcogenide conversion by removing the disproportionation reaction product of Na₂TeO₃ through reacting with EG. In addition, we observe that a higher reaction temperature in scale-up SCS also enables the formation of slightly larger particles (1.87 \pm 0.40

μm), whereas the particles formed from scale-up ECS and HCS have a size of 1.64 \pm 0.41 μm and 0.93 \pm 0.17 μm , respectively. These results confirm the critical role of reaction conditions (e.g., solvent and temperature) in the scale-up synthesis of metal telluride nanoplates.

To quantify the scalability of the SCS approach, we further study the reaction kinetics over different precursor amounts and reaction times. In a small-batch synthesis, a batch of 6 mmol Sb precursors (e.g., SbCl₃) was used to produce around

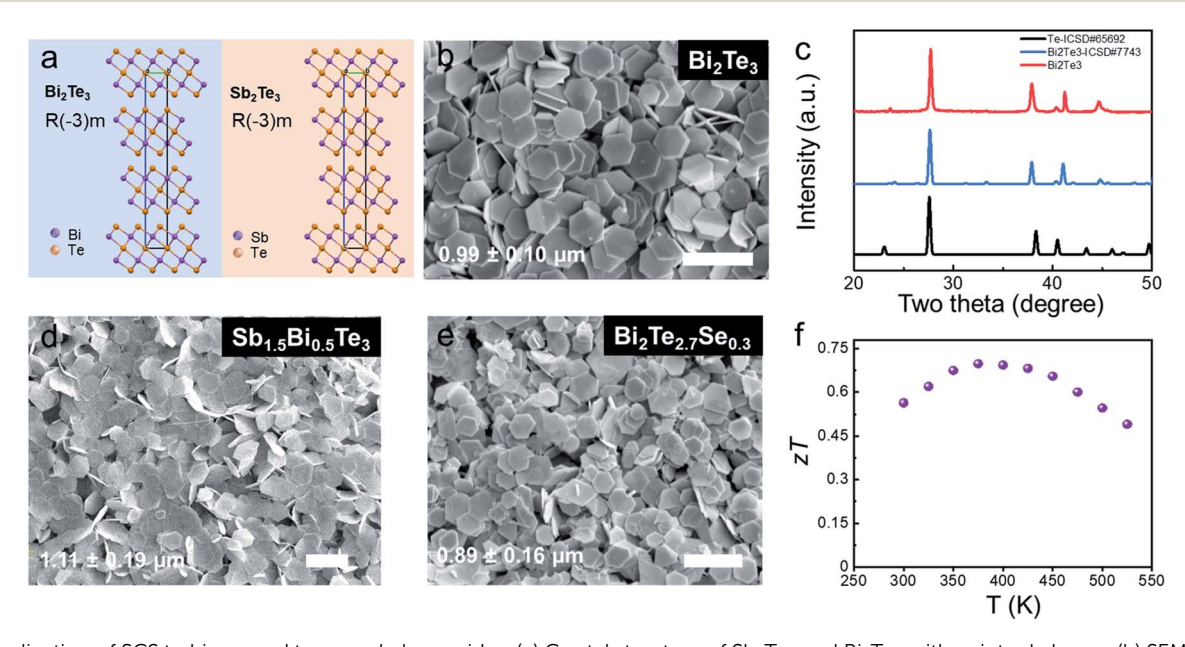


Fig. 3 Application of SCS to binary and ternary chalcogenides. (a) Crystal structure of Sb₂Te₃ and Bi₂Te₃ with quintuple layers. (b) SEM image of Bi_2Te_3 nanoplates made by the SCS method. (c) XRD of Bi_2Te_3 nanoplates confirming the pure phase without Te impurity. (d and e) SEM image of ternary chalcogenide Sb_{1.5}Bi_{0.5}Te₃ (d) and Bi₂Te_{2.7}Se_{0.3} (e) made by the SCS method. (f) Thermoelectric ZT of n-type ternary chalcogenide nanoplates. Scale bars are 2 µm.

3 mmol Sb₂Te₃ of nanoplates in 12 h. As shown in XRD data (Fig. 2f), a 300% scale-up synthesis shows no Te signal, while some impurity starts to emerge as the batch size increases to a 900% batch. Nevertheless, such Te impurity can be completely eliminated by prolonging the reaction time to 24 h, leading to an impurity-free synthesis of Sb₂Te₃ nanoplates. In addition to Sb₂Te₃ nanoplates, Bi₂Te₃ shares the same crystal structure (space group $R\bar{3}m$) with Sb₂Te₃ (Fig. 3a), and thus we hypothesize that such scale-up synthesis can also be applicable to Bi₂Te₃ syntheses. As shown in Fig. 3b, SEM images reveal a hexagonal morphology of Bi₂Te₃ without any observable Te nanowires, which is confirmed using XRD analysis (shown in Fig. 3c). Similarly, binary bismuth selenide (Bi₂Se₃) nanoplates have also been prepared with no observable impurity (Fig. S1†). Noticeably, such colloidal synthesis is not limited to binary chalcogenide systems, but also applicable to more sophisticated composition. As a proof of concept of synthesizing ternary chalcogenides, the SCS method was employed to prepare purephase Sb_{1.5}Bi_{0.5}Te₃ (Fig. 3d) and Bi₂Te_{2.7}Se_{0.3} (Fig. 3e), where no Te impurity was observed in the above systems as evidenced by XRD analyses. Furthermore, to evaluate the transport properties of MMCs, the scale-up synthesized Bi₂Te_{2.7}Se_{0.3} nanoparticles were consolidated into a pellet using spark plasma sintering (SPS), followed by thermoelectric property measurements (Fig. S2†). With a room-temperature electrical conductivity of \sim 60 000 S m⁻¹, the pellet sample demonstrated a peak ZT of 0.7 at 375 K (Fig. 3f), which are comparable to those of some wetchemistry synthesized n-type Bi₂Te₃-based chalcogenides reported in the literature. ^{24,28,29}

To implement chalcogenide inks in additive manufacturing, the ink stability is a crucial factor. We hypothesize that the ink stability depends on several factors including solvents, additives, and pH values, and we further study and optimize ink formulations to prolong the chalcogenide nanoplate's chemical stability (Fig. 4a). It is worth mentioning that our goal is not to completely prevent the particle oxidation; instead, we aim to qualitatively understand the collective behavior of chalcogenide nanoplates under different ink factors in order to mitigate such oxidation processes. Using Bi₂Te_{2,7}Se_{0,3} as an example, different ink formulations have been systematically investigated including ink solvent, oxygen scavengers, and pH modifiers (Fig. 4b). We select water as a reference ink solvent as it has been widely used in various printing techniques (e.g., inkjet printing).30 Ethylene glycol is also tested to examine the solvent effect on particle stability. Vitamin C (VC) and ethyl gallate (EGL) are popular oxygen scavengers used in the food industry,31,32 and thus are also tested in our experiments (vitamin C was neutralized with NH₃·H₂O to a pH of ~7 before adding to the chalcogenide system). It has been shown that the ink solvent can significantly affect the long-term stability of the inks, where Bi₂Te_{2.7}Se_{0.3} particles in ethylene glycol show the highest stability, showing a 6 fold improvement in electrical conductivity compared to that of conventional water-based ink formulation. VC-based inks also show good stability and demonstrate the second lowest electrical resistivity. For the

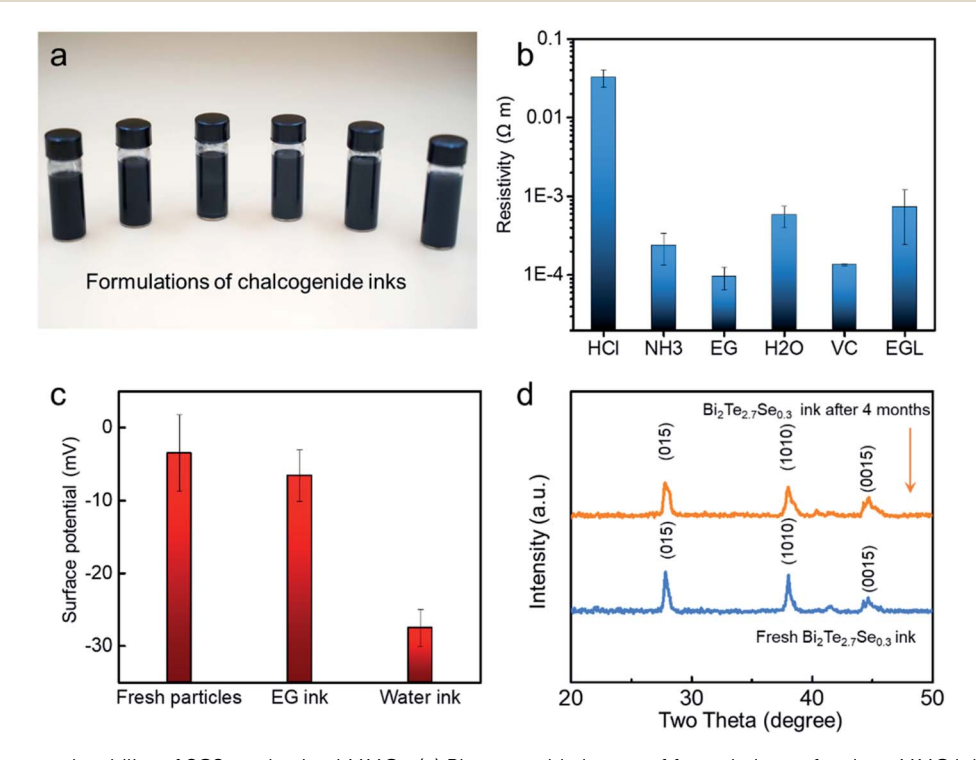


Fig. 4 Ink formulations and stability of SCS synthesized MMCs. (a) Photographic image of formulations of various MMC inks. From left to right: HCl, NH₃, EG, water, vitamin C, and ethyl gallate inks. (b) Resistivity of MMC particles stored in various inks for a period of time (45 days). (c) Zeta potential measurements of fresh ink, EG ink, and water ink of $Bi_2Te_{2.7}Se_{0.3}$ for a period of time (4 months). (d) XRD analysis of fresh and EG ink of $Bi_2Te_{2.7}Se_{0.3}$ for a period of storage time (4 months).

sample with HCl solution, we observed a high resistivity of Bi₂Te_{2.7}Se_{0.3} particles in an acidic environment, which suggests that acids should be avoided in chalcogenide ink formulation. To our surprise, the EGL-based ink seems to produce relatively resistive films and such high resistivity is likely due to the formation of an insulating polymer layer on Bi₂Te_{2.7}Se_{0.3} particles, as evidenced by other polyphenol systems where the oxidation of phenols (such as EGL) often leads to oxidative polymerization.33,34

To further understand the stabilization mechanism of EGbased ink formulation, we examined the surface charging group of Bi₂Te_{2.7}Se_{0.3} particles through in situ characterization of the surface charge in the ink stage using zeta potential techniques. For freshly made Bi2Te2.7Se0.3 particles, we observed a slightly negative value of -3.52 ± 5.24 mV at neutral pH, which is comparable to other chalcogenide nanoplate systems.35 After long-term storage in water (120 days), we observed that the surface potential of water-based inks sharply plummets to -27.51 ± 2.59 mV (Fig. 4c), which indicates the formation of negatively charged groups such as -OH.36-38 By contrast, the EG-based ink only shows a slight decrease in surface potential to -6.58 ± 3.52 mV. In addition, sedimentation analyses of water-based and EG-based inks (Fig. S3†) reveal a fast sedimentation of Bi₂Te_{2.7}Se_{0.3} particles in water-based inks in less than 0.5 h, whereas no observable sedimentation was seen for EG-based inks primarily due to the high viscosity of EG as the sedimentation coefficient is inversely proportional to solvent viscosity. To verify the phase stability of chalcogenide nanoplates, we performed a comparative analysis on the Bi₂-Te_{2.7}Se_{0.3} particles before and after long-term storage in EG (4 months). As shown in the XRD data (Fig. 4d), there is no significant shift in the peak position or new impurity peaks, indicating decent chemical stability of the EG-based ink. The improved stability of chalcogenide particles is attributed to the ability of ethylene glycol to effectively quench reactive oxygen species (ROS).39,40 In fact, ethylene glycol has been widely used to reduce metal precursors to metals such as Ag and Pd at room temperature.41,42

Having demonstrated the long-term stability of EG-based chalcogenide inks, we investigated the compatibility of our inks with different additive manufacturing methods including aerosol jet printing and extrusion printing techniques (Fig. 5a). We first tested the printability of EG-based inks using extrusion printing. As shown in Fig. S4,† several high-quality films can be readily printed without a significant undesired "coffee ring" effect. The printability of inks with high particle concentrations (up to 43 wt%) was tested and no severe clogging was observed due to minimal aggregation or agglomeration of the particles. Despite the intrinsic high viscosity of EG, it is worth mentioning that the EG-based ink can also be printed using other printing methods requiring relatively low ink viscosities by judiciously designing the ink rheology (such as mixing with low viscosity solvents). For example, ultrasonic-based aerosol-jet printing (UAJP) techniques typically handle inks with a viscosity <30 cP.43-45 The EG-based ink diluted with water with a 1:5.7 ratio can also be easily printed via UAJP into high resolution patterns on 2D and 3D curved substrates (Fig. 5b). As shown in Fig. 5c, a 2D pattern with a line width <0.1 mm was readily realized via a single printing pass. Fig. 5d shows a 3D conformal architecture by printing MMC inks on a 3D hemisphere, which further confirms the high printability of MMC particles. While the detailed printed device performance is out of the scope of this article, the extrusion printed n-type Bi₂Te_{2.7}Se_{0.3} film (24.7 μm in thickness) shows a room-temperature thermoelectric power factor of 662.9 µW m⁻¹ K⁻², which is comparable to that of printed chalcogenide systems (Fig. 5e and Table S2†).46-51 In

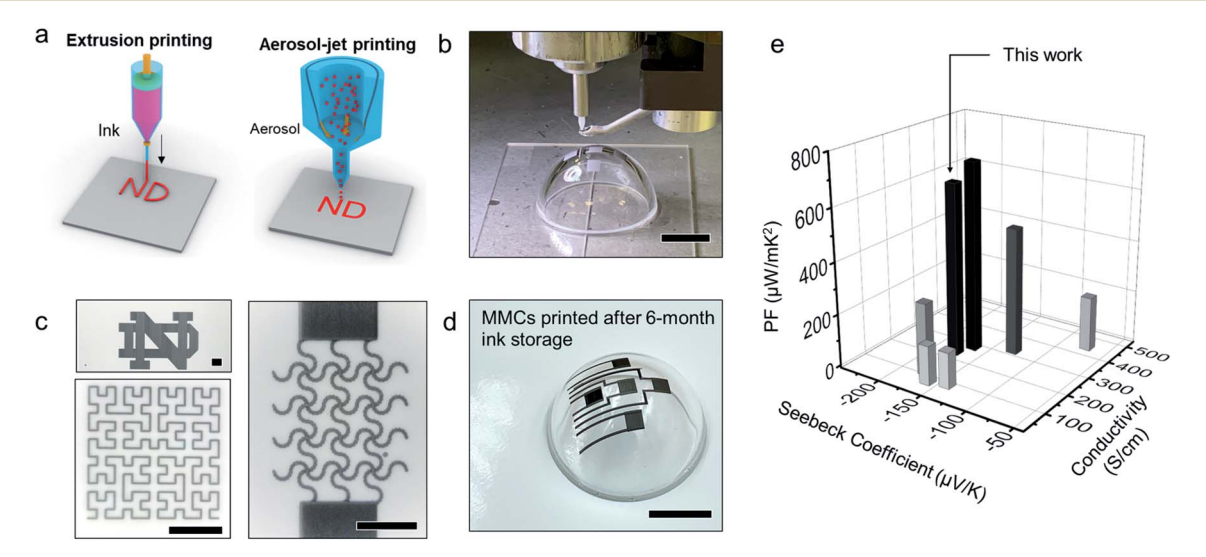


Fig. 5 Ink printability of SCS synthesized MMCs. (a) Schematic illustration of two additive manufacturing processes including extrusion and aerosol jet printing. (b) Photographic image showing the aerosol jet printing process on a curved glass dome using MMC inks. Scale bar: 1 cm. (c) Several printed 2D patterns with a high spatial resolution (as small as 50 µm in line width). Scale bars: 2 mm. (d) Photographic examples of 3D printed ternary chalcogenide nanoplates, showing excellent printability and processability even after 6 month ink storage. Scale bar: 1 cm. (e) Comparison of the thermoelectric power factor of different printed n-type TE films (values from ref. 46-51).

future, device optimization and system integration would be desirable to complement the synthetic efforts to accelerate the broad application of semiconducting chalcogenide particles.

In summary, we investigated a hydrazine-free, phase-pure, and scalable approach for synthesizing and processing main group chalcogenides with an emphasis of V-VI nanoplates. We quantitatively compared the scale-up syntheses via hydrazinebased and hydrazine-free wet chemistry, and provided a systematic analysis on the scalability of chalcogenide synthesis. Upon scaling up the reaction, we observed the formation of byproduct tellurium during the MMC synthesis and correlated it with incomplete chalcogenide conversion. We demonstrated the role of applying classic Le Chatelier's principle and reaction kinetics in addressing the byproduct tellurium during the synthesis in a larger batch. By screening a number of ink factors including solvent, additives, and pH values, we investigated the effect of different ink formulations on MMCs and demonstrated an EG-based chalcogenide ink with long-term chemical stability in an ambient environment. Combining highly scalable syntheses and judicious design of ink formulation could provide important insights toward largescale applications of main group chalcogenide-based nanomaterials.

Methods

Materials

Sodium hydroxide, sodium tellurite, tellurium dioxide, selenium dioxide, antimony trichloride, bismuth(III) nitrate pentahydrate, polyvinylpyrrolidone (PVP, 40 000 g mol⁻¹), ethylene glycol, and diethylene glycol were obtained from Sigma Aldrich (USA).

Hydrazine-based colloidal synthesis (HCS)

The scale-up synthesis of MMC nanoparticles was performed by strictly increasing the amount of starting materials by 300% from our previous work. In a typical synthesis of Sb₂Te₃, 210 mL ethylene glycol (EG) solution containing mixed antimony trichloride (SbCl₃, 18 mmol), tellurium dioxide (TeO₂, 27 mmol), sodium hydroxide (NaOH, 4.5 g), and PVP ($M_{\rm s} \approx 40~000~{\rm g~mol^{-1}}$, 2.4 g) was heated to 110 °C. 30 mL hydrazine hydrate was swiftly injected. The mixture was maintained at 130 °C for 30 min, and then heated under reflux for 12 h. The particles were collected by centrifugation at 5000 rpm, and washed using ethanol another three times.

Ethylene-assisted colloidal synthesis (ECS)

In the ECS method, there is no hydrazine involved during the entire synthesis process. In a typical synthesis of Sb_2Te_3 , 210 mL ethylene glycol (EG) solution containing mixed antimony trichloride (SbCl₃, 18 mmol), tellurium dioxide (TeO₂, 27 mmol), sodium hydroxide (NaOH, 4.5 g), and PVP ($M_s \approx 40\,000$ g mol⁻¹, 2.4 g) was heated under reflux for 12 h. The particles were collected by centrifugation at 5000 rpm, and washed using ethanol another three times.

Solvent-engineered colloidal synthesis (SCS)

The metal telluride particles were prepared by introducing a mixture of diethylene glycol and ethylene glycol. Taking the 300% scale-up synthesis of Sb₂Te₃ nanoplates as an example, antimony trichloride (SbCl3, 18 mmol), sodium tellurite (Na₂TeO₃, 27 mmol), sodium hydroxide (NaOH, 5 g), and PVP (M_s $\approx 40~000~\mathrm{g~mol}^{-1}$, 2.4 g) were added to 230 mL mixed solvent of ethylene glycol and diethylene glycol (1:2). The mixture was heated under reflux for 12 to 24 h. The particles were collected by centrifugation at 5000 rpm and washed using ethanol another three times. For 300% scale-up synthesis of Bi₂Te₃ nanoplates, bismuth nitrate pentahydrate (Bi(NO₃)₃·5H₂O, 18 mmol), sodium tellurite (Na₂TeO₃, 27 mmol), sodium hydroxide (NaOH, 5 g), and PVP ($M_s \approx 40~000~{\rm g~mol^{-1}}$, 2.4 g) were added to 200 mL mixed solvent of ethylene glycol and diethylene glycol (4:1). The mixture was heated under reflux for 12 to 24 h. The particles were collected by centrifugation at 5000 rpm and washed using ethanol another three times. For the synthesis of 1D tellurium nanowires, only sodium tellurite was used without the addition of antimony trichloride while keeping the other conditions unchanged. Under our experimental conditions, we found that the SCS method can be scale up to a 54 mmol batch of metal precursors, which corresponds to a yield of Sb₂Te₃ and Bi₂Te₃ of approximately 15 g and 20 g per batch, respectively.

Ink formulation

In a typical ink formulation, solvents, pH modifiers, and additives were used to formulate thermoelectric inks in 2 mL polypropylene tubes. For ink solvents, water and ethylene glycol were tested. For pH modifiers, 0.1 M HCl or 0.1 M NH₃ solution was added to inks to provide an acidic or alkaline environment. Vitamin C (1 wt%) or ethyl gallate (1 wt%) was selected as the oxygen scavenger in inks. The dispersion was sonicated using a bath sonicator for 15 min to ensure the homogeneous dispersion of inks without aggregation. After a certain period of storage time, the chalcogenide particles were collected by centrifugation at 5000 rpm and washed using deionized water and ethanol three times prior to resistivity measurements. The lateral size of the chalcogenide particles was characterized by SEM analyses. No aggregation was observed when the ink was transferred into the ink cartridge or during printing.

Printing, cold pressing, and sintering

In a typical printing process, we tested the printability of MMC inks using both an aerosol jet printer and an extrusion printer. For aerosol jet printing, an ultrasonic atomizer was used to aerosolize the ink, which was then carried to the deposition head by an inert carrier gas flow (N_2). In the deposition head, the aerosolized ink flow is focused and directed to the substrate through a nozzle. Printing parameters are given in the ESI (Table S3†). For extrusion printing, a home-built printer with a pneumatically controlled extrusion process was used. The extrusion apparatus mainly consists of an ink cartridge and an extrusion needle of 22 gauge. To ensure the uniform density of the printed film, systemic optimization of the extrusion

pressure was performed ahead of printing the nanoplate ink. The approximate size of the printing was maintained at 15 mm \times 2 mm with a 3.5 mm s⁻¹ speed and 0.2 mm gap between adjacent layers. The printed TE film was completely dried in a furnace at 250 °C for 1 h prior to cold pressing twice at 20 MPa for 5 minutes. The dried and cold-pressed TE film is then sintered in an inert environment (N₂/H₂) at 450 °C for 1 h.

A focused ion beam-scanning electron microscope (FIB-SEM,

Characterization

Helios G4 UX) was used to obtain the SEM images of samples. The room temperature Seebeck coefficient and electrical conductivity are measured using a custom-built setup. We used the four-point probe method for electrical conductivity measurement. The printed TE film is placed on a dielectric substrate (glass slide) with two electrodes on both ends, in which current is supplied for electrical conductivity measurement. We used high electrical conductivity silver adhesive (503 Electron Microscopy Sciences) for connecting current electrodes to the film. Two k-type thermocouples (40 AWG) are connected to the film using dielectric probes. The probes provide sufficient pressure on thermocouples (TCs) to maintain a good contact between the TE film and TCs without causing any damage to the film. The voltage is measured across the negative leads of the thermocouples using a data acquisition system (Keysight 34970A). This is done for six equally spaced currents. The sample resistance *R* is the slope of the best fit line through the V/I data and the conductivity is then calculated as $\sigma = \frac{L}{RA}$. where L is the distance between the thermocouple tips and A is the cross-sectional area of the TE film. We used a 2D profilometer (DektakXT stylus profilometer, Bruker, US) to measure the thickness of the film at five different locations and used the average value to calculate the cross-sectional area. For Seebeck coefficient measurement, one end of the film is placed on a heater and the other end on a heat sink. The temperature gradient ΔT is measured using TCs. Seebeck coefficient measurement begins by slowly ramping the temperature gradient ΔT from \sim 0 K to about 6 K, while recording ΔT and the voltage difference ΔV across the negative leads of the TCs using a data acquisition system. The negative of the slope of the best fit line through the $\Delta V/\Delta T$ data gives the Seebeck coefficient relative to the material comprising the negative lead of the thermocouple $\left(S = \frac{-\Delta V}{\Delta T}\right)$. The absolute Seebeck coefficient of

the sample is obtained by adding the absolute Seebeck coefficient of the negative thermocouple wire material to the measured sample relative Seebeck coefficient. For Seebeck coefficient measurement, the instrument was calibrated using a standard constantan sample of known properties. The measurement error of the home-built set-up was \sim 5% for both the electrical conductivity and the Seebeck coefficient.

Conflicts of interest

The authors declare no competing interests.

Acknowledgements

Y. Z. would like to acknowledge financial support from the National Science Foundation under award CMMI-1747685, and the U.S. Department of Energy under awards DE-EE0009103 and DE-NE0008812. At Northwestern the work was supported mainly by the Department of Energy, Office of Science Basic Energy Sciences under grant DE-SC0014520, and DOE Office of Science (TE measurements).

References

- 1 F. Kim, B. Kwon, Y. Eom, J. E. Lee, S. Park, S. Jo, S. H. Park, B.-S. Kim, H. J. Im, M. H. Lee, T. S. Min, K. T. Kim, H. G. Chae, W. P. King and J. S. Son, Nat. Energy, 2018, 3, 301-309
- 2 S. Li, X. Li, Z. Ren and Q. Zhang, J. Mater. Chem. A, 2018, 6, 2432-2448.
- 3 X. Wang, H. Wang, W. Su, T. Wang, M. A. Madre, J. Zhai, T. Chen, A. Sotelo and C. Wang, J. Mater. Chem. A, 2020, 8, 3379-3389.
- 4 W. Zheng, T. Xie, Y. Zhou, Y. L. Chen, W. Jiang, S. Zhao, J. Wu, Y. Jing, Y. Wu, G. Chen, Y. Guo, J. Yin, S. Huang, H. Q. Xu, Z. Liu and H. Peng, Nat. Commun., 2015, 6, 6972.
- 5 F. Brückerhoff-Plückelmann, J. Feldmann, C. D. Wright, H. Bhaskaran and W. H. P. Pernice, J. Appl. Phys., 2021, 129, 151103.
- 6 J. Feldmann, N. Youngblood, M. Karpov, H. Gehring, X. Li, M. Stappers, M. Le Gallo, X. Fu, A. Lukashchuk, A. S. Raja, J. Liu, C. D. Wright, A. Sebastian, T. J. Kippenberg, W. H. P. Pernice and H. Bhaskaran, *Nature*, 2021, **589**, 52–58.
- 7 C. Han, Q. Sun, Z. Li and S. X. Dou, Adv. Energy Mater., 2016, 6, 1600498.
- 8 Y. Zhang, S. Hao, L.-D. Zhao, C. Wolverton and Z. Zeng, J. Mater. Chem. A, 2016, 4, 12073-12079.
- 9 H. Ju, D. Park and J. Kim, J. Mater. Chem. A, 2018, 6, 5627-5634.
- 10 C. Zhou, Y. K. Lee, Y. Yu, S. Byun, Z.-Z. Luo, H. Lee, B. Ge, Y.-L. Lee, X. Chen, J. Y. Lee, O. Cojocaru-Mirédin, H. Chang, J. Im, S.-P. Cho, M. Wuttig, V. P. Dravid, M. G. Kanatzidis and I. Chung, Nat. Mater., 2021, 20, 1378-1384.
- 11 J. Fan, X. Wang, F. Liu, Z. Chen and G. Chen, ACS Appl. Mater. Interfaces, 2021, 13, 30731-30738.
- 12 J. Fan, X. Huang, F. Liu, L. Deng and G. Chen, Compos. Commun, 2021, 24, 100612.
- 13 F. Rao, K. Ding, Y. Zhou, Y. Zheng, M. Xia, S. Lv, Z. Song, S. Feng, I. Ronneberger, R. Mazzarello, W. Zhang and E. Ma, Science, 2017, 358, 1423.
- 14 M. Salinga, B. Kersting, I. Ronneberger, V. P. Jonnalagadda, X. T. Vu, M. Le Gallo, I. Giannopoulos, O. Cojocaru-Mirédin, R. Mazzarello and A. Sebastian, Nat. Mater., 2018, 17, 681-
- 15 W. Zhang and E. Ma, Nat. Mater., 2018, 17, 654-655.
- 16 C. Chen and J. Tang, ACS Energy Lett., 2020, 5, 2294–2304.
- 17 M. Zeng, M. Chen, D. Huang, S. Lei, X. Zhang, L. Wang and Z. Cheng, Mater. Horiz., 2021, 8, 758-802.

- 18 S. Bukkapatnam, S. Kamarthi, Q. Huang, A. Zeid and R. Komanduri, *IIE Trans.*, 2012, 44, 492–495.
- 19 L. Xu, L. Wang and Q. Huang, IIE Trans., 2015, 47, 274-284.
- 20 C. Gu, H.-M. Xu, S.-K. Han, M.-R. Gao and S.-H. Yu, *Chem. Soc. Rev.*, 2021, **50**, 6671–6683.
- 21 C. Dun, W. Kuang, N. Kempf, M. Saeidi-Javash, D. J. Singh and Y. Zhang, *Adv. Sci.*, 2019, **6**, 1901788.
- 22 G. Zhang, W. Wang, X. Lu and X. Li, *Cryst. Growth Des.*, 2009, 9, 145–150.
- 23 H. Q. Yang, L. Miao, C. Y. Liu, C. Li, S. Honda, Y. Iwamoto, R. Huang and S. Tanemura, *ACS Appl. Mater. Interfaces*, 2015, 7, 14263–14271.
- 24 R. Jin, G. Chen, J. Pei, H. Xu and Z. S. Lv, *RSC Adv.*, 2012, 2, 1450–1456.
- 25 B. Zhou, Y. Ji, Y.-F. Yang, X.-H. Li and J.-J. Zhu, Cryst. Growth Des., 2008, 8, 4394–4397.
- 26 K. Takahashi, S. Yokoyama, T. Matsumoto, J. L. Cuya Huaman, H. Kaneko, J.-Y. Piquemal, H. Miyamura and J. Balachandran, *New J. Chem.*, 2016, **40**, 8632–8642.
- 27 K. J. Carroll, J. U. Reveles, M. D. Shultz, S. N. Khanna and E. E. Carpenter, J. Phys. Chem. C, 2011, 115, 2656–2664.
- 28 J. Jiang, L. Chen, S. Bai, Q. Yao and Q. Wang, J. Mater. Sci. Eng. B, 2005, 117, 334–338.
- 29 M. Imamuddin and A. Dupre, *Phys. Status Solidi A*, 1972, **10**, 415–424.
- 30 D. McManus, S. Vranic, F. Withers, V. Sanchez-Romaguera, M. Macucci, H. Yang, R. Sorrentino, K. Parvez, S.-K. Son, G. Iannaccone, K. Kostarelos, G. Fiori and C. Casiraghi, *Nat. Nanotechnol.*, 2017, 12, 343.
- 31 T. Kalaivani, C. Rajasekaran and L. Mathew, *J. Food Sci.*, 2011, 76, T144–T149.
- 32 S. Mohan, K. Thiagarajan and R. Chandrasekaran, *Biochem. J.*, 2017, 474, 3011–3025.
- 33 G. D. Cooper and J. G. Bennett, *J. Org. Chem.*, 1972, 37, 441–447.
- 34 L. Panzella and A. Napolitano, Antioxidants, 2017, 6, 30.

- 35 X. Lu, Q. Zhang, J. Liao, H. Chen, Y. Fan, J. Xing, S. Gu, J. Huang, J. Ma, J. Wang, L. Wang and W. Jiang, Adv. Energy Mater., 2020, 10, 1902986.
- 36 Y.-W. Lai and W.-C. J. Wei, Materials, 2016, 9, 863.
- 37 M. Zeng, S. A. Shah, D. Huang, D. Parviz, Y.-H. Yu, X. Wang, M. J. Green and Z. Cheng, ACS Appl. Mater. Interfaces, 2017, 9, 30797–30804.
- 38 R. Ma, M. Zeng, D. Huang, J. Wang, Z. Cheng and Q. Wang, *J. Colloid Interface Sci.*, 2021, **601**, 106–113.
- 39 S. C. Bondy and S. Naderi, *Biochem. Pharmacol.*, 1994, 48, 155–159.
- 40 H. M. Jalali, RSC Adv., 2014, 4, 32928-32933.
- 41 D. Chen, X. Qiao, X. Qiu and J. Chen, *J. Mater. Sci.*, 2009, 44, 1076–1081.
- 42 L.-J. Chen, C.-C. Wan and Y.-Y. Wang, *J. Colloid Interface Sci.*, 2006, 297, 143–150.
- 43 M. Zeng and Y. Zhang, J. Mater. Chem. A, 2019, 7, 23301-23336.
- 44 M. Zeng, W. Kuang, I. Khan, D. Huang, Y. Du, M. Saeidi-Javash, L. Zhang, Z. Cheng, A. J. Hoffman and Y. Zhang, Adv. Mater., 2020, 32, e2003081.
- 45 M. Saeidi-Javash, Y. Du, M. Zeng, B. C. Wyatt, B. Zhang, N. Kempf, B. Anasori and Y. Zhang, ACS Appl. Electron. Mater., 2021, 3, 2341–2348.
- 46 T. Varghese, C. Hollar, J. Richardson, N. Kempf, C. Han, P. Gamarachchi, D. Estrada, R. J. Mehta and Y. Zhang, *Sci. Rep.*, 2016, 6, 33135.
- 47 A. Chen, D. Madan, P. K. Wright and J. W. Evans, *J. Micromech. Microeng.*, 2011, 21, 104006.
- 48 D. Madan, Z. Wang, A. Chen, R.-c. Juang, J. Keist, P. K. Wright and J. W. Evans, *ACS Appl. Mater. Interfaces*, 2012, 4, 6117–6124.
- 49 M. Saeidi-Javash, W. Kuang, C. Dun and Y. Zhang, *Adv. Funct. Mater.*, 2019, 29, 1901930.
- 50 S. Ferhat, C. Domain, J. Vidal, D. Noël, B. Ratier and B. Lucas, *Org. Electron.*, 2019, **68**, 256–263.
- 51 Y. Wang, G. Liu, M. Sheng, C. Yu and Y. Deng, *J. Mater. Chem. A*, 2019, 7, 1718–1724.